Development of experimental and numerical methods for the analysis of active clearance control systems

Riccardo Da Soghe
Ergon Research,
via Campani 50,
Florence 50127, Italy
e-mail: riccardo.dasoghe@ergonresearch.it

Lorenzo Mazzei
Ergon Research,
via Campani 50,
Florence 50127, Italy
e-mail: lorenzo.mazzei@ergonresearch.it

Lorenzo Tarchi
Ergon Research,
via Campani 50,
Florence 50127, Italy
e-mail: lorenzo.tarchi@ergonresearch.it

Lorenzo Cocchi[2]
Department of Industrial Engineering,
University of Florence,
via S. Marta 3,
Florence 50139, Italy
e-mail: lorenzo.cocchi@htc.unifi.it

Alessio Picchi
Department of Industrial Engineering,
University of Florence,
via S. Marta 3,
Florence 50139, Italy
e-mail: alessio.picchi@htc.unifi.it

Bruno Facchini
Department of Industrial Engineering,
University of Florence,
via S. Marta 3,
Florence 50139, Italy
e-mail: bruno.facchini@htc.unifi.it

Laurent Descamps
Safran Aircraft Engines,
Villaroche,
Réau 77550, France
e-mail: laurent.descamps@safrangroup.com

Julian Girardeau
Safran Aircraft Engines,
Villaroche,
Réau 77550, France
e-mail: julian.girardeau@safrangroup.com

Matthieu Simon
Safran Aircraft Engines,
Villaroche,
Réau 77550, France
e-mail: matthieu.simon@safrangroup.com

Development of Experimental and Numerical Methods for the Analysis of Active Clearance Control Systems[1]

The ever increasing performance requirements of modern aeroengines necessitate the development of effective ways to improve efficiency and reduce losses. Casing temperature control is particularly critical from this point of view, since thermal expansion directly affects the blade tip clearance and thus the associated leakages. To limit the turbine tip flows, active clearance control (ACC) systems have been implemented over the last decades. These systems are usually based upon impingement cooling, generated by a series of perforated manifolds enclosing the turbine casing. When dealing with aeroengine low pressure turbines, the current trend in increasing the engine bypass ratio, so as to enhance the system propulsive efficiency, pushes the limits of ACC traditional design performance. The reduction of the pressure head at the ACC system inlet requires lower nozzle-to-target distances as well as denser impingement arrays to compensate the reduction of the jets' Reynolds number. Literature correlations for the impingement heat transfer coefficient estimation are then out of their confidence range and also RANS numerical approaches appear not suitable for future ACC designs. In this work, methodologies for the development of accurate and reliable tools to determine the heat transfer characteristics of low pressure ACC systems are presented. More precisely, this paper describes a custom designed finite difference procedure capable of solving the inverse conduction problem on the target plate of a test sample. The methodology was successfully applied to an experimental setup for the measurement of the thermal loads on a target plate of a representative low pressure ACC impinging system. The experimental outcomes are then used to validate a suitable numerical approach. Results show that RANS model is not able to mimic the experimental trends, while scale-resolving turbulence models provide a good reconstruction of the experimental evidences, thus allowing to obtain a correct interpretation of flow and thermal phenomena for ACC systems.
[DOI: 10.1115/1.4049354]

Introduction

General Overview. The control of tip leakages in low pressure turbine (LPT) is a fundamental task to optimize the turbine module efficiency. This statement is motivated by two evidences: the flows evolving through the outer ring cavities do not contribute to the power generation, and the tip cavity region egress interacts with the main annulus flow, introducing spoiling effects that

[1]ASME TURBO EXPO 2020 Turbomachinery Technical Conference and Exposition, September 21–25, 2020, Virtual Conference, Online.
[2]Corresponding author.
Manuscript received September 8, 2020; final manuscript received September 21, 2020; published online January 28, 2021. Editor: Jerzy T. Sawicki.

further deteriorate the stage efficiency. Aircraft engines are exposed to extremely variable centrifugal and thermal loads during their mission. As a consequence, clearances at the engine outer rings, as well as clearances under LPT nozzles, can be strongly variable. Such dimensional variation may worsen engine performance and reduce the components' life span. In order to mitigate clearances variations, the active control of engine LPT casing temperature, generally based on impingement cooling, is a common practice. Jets are directed toward the external turbine casing by means of a series of circumferential feeding pipes (Fig. 1). The amount of impinging cooling flow is real-time regulated with a control valve driven by a specific logic implemented in the full authority digital engine control. The final aim is to keep the clearances between blades tips and casing as close as possible across the different engine operating conditions and mainly during cruise operation. In most designs, to avoid or reduce parasitic effects on the engine cycle performance, feeding air for the active clearance control (ACC) system of the LPT is generally extracted from the secondary bypass flow. The current trend in increasing the engine bypass ratio, to enhance the system propulsive efficiency, pushes the limits of ACC traditional design performance. In fact, the downside of the increased bypass ratio is that the fan pressure ratio tends to fall, thus reducing the pressure ratio on the low pressure turbine ACC (LPTACC). In this way, a more efficient and effective ACC supply system is needed, reducing the overall internal piping drag and improving the air scoop designs. Beside these improvements, the reduction of the pressure head at the ACC system inlet requires lower nozzle-to-target distances as well as denser impingement arrays to compensate for the reduction of the jets' Reynolds number (Re_j). For these applications, the Re_j can be lower than 2000, potentially making relevant the transitional effects and the presence of geometrical imperfections (which could result in turbulence promotors). This new scenario introduces further complexities in the design of future LPTACC arrangements from both system mechanical integrity and thermal management perspectives.

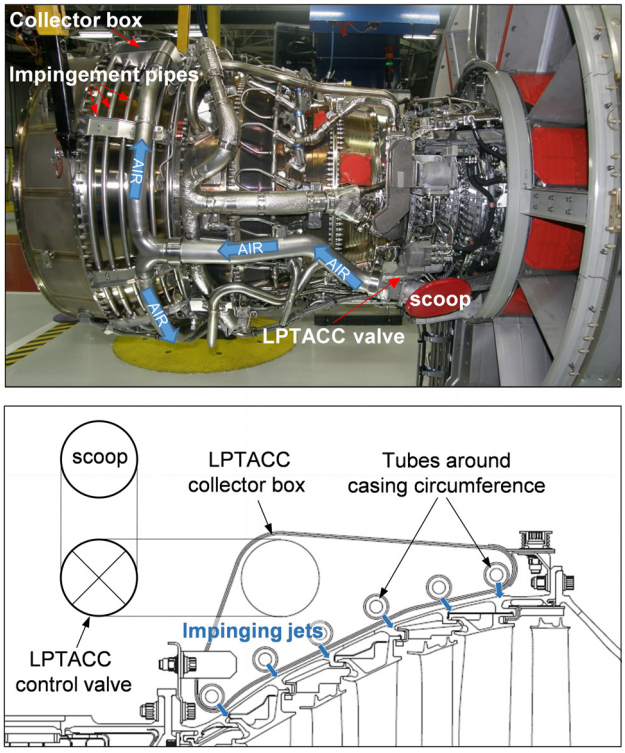

Fig. 1 CFM56-5B LPTACC system (up), LPTACC functional sketch (down)—Safran Aircraft Engines

Literature Review. There are several challenges in the LPTACC traditional design, spanning from the impingement holes discharge behavior to the impingement jet heat transfer performance. Interesting discussions on this can be found in Da Soghe et al. [1–7].

As far as the mass flow rate split across the manifold is concerned, many parameters may influence the discharge coefficient (C_d) of the impinging holes [8]. Several studies have been carried out on different geometries of holes subjected to a wide range of fluid-dynamic conditions. This allowed to produce suitable correlations to predict the discharge behavior; an extensive review can be found in Hay and Lampard [9]. Despite the interest on the problem, most of the literature contributions focus on a single hole arrangement (see as an example Refs. [10–13]) or on global discharge coefficient related to jet array configurations [14–17]. Very few correlations are available in the open literature to calculate the hole discharge coefficient of a single hole in a jet array. In this way, interesting contributions come from Da Soghe and Andreini [1,2]: basing on LPTACC real engine arrangements, the authors sorted out a dataset of cylindrical feeding pipes with impingement holes to correlate the C_d of each jet of the array. The developed correlation was obtained exploiting data in a wide range of operating conditions ($2000 \leq \mathrm{Re}_j \leq 12{,}000$, $1.01 \leq \beta \leq 1.6$).

Focusing on the target plate heat transfer, measurements on multiple jet impingement arrays can be found in a variety of existing publications (see as example Refs. [17–22]). As far as ACC arrangements are concerned, interesting contributions come from Ahmed et al. [23–25] who performed some studies of the flow in representative ACC system conditions. These studies are aimed at the prediction of impingement jet characteristics in form of discharge coefficients, local and spatially averaged Nusselt numbers and heat transfer coefficients. The configurations tested by Ahmed et al. are characterized by a Re_j of 7500. Similar results were obtained by Merzec and Kucabba-Pietal [26] ($\mathrm{Re}_j = 5000$, without experimental data to support the computational fluid dynamics (CFD) results). In the studies above, it was claimed that the exploited RANS CFD approach (k-ω SST two-equation turbulence model) was capable of reproducing reliable heat transfer rates. The main limiting aspect of these interesting contributions consists in the fact that the authors do not evaluate the effects of the undercowl flow on the impingement jets (or only consider the interaction between the jets and a quiescent environment through CFD). Andreini et al. [3] conducted an analysis aimed at the study of the heat transfer and the adiabatic effectiveness on LPTACC of a commercial aeroengine which implements 5 ACC rails ($6500 \leq \mathrm{Re}_j \leq 10{,}500$). The study underlines the effects of the undercowl flow on the impingement jets also, and numerical calculations were proposed to point out if CFD is able to confidently reproduce the experimental evidences. It was demonstrated that the effect of the undercowl flow on the target plate heat transfer is noticeable at the first ACC rails only. The agreement between the CFD (RANS approach) and the experiments is good at high Re_j while worsens in case of low Re_j. More precisely, for the minimum jet flowrate ($\mathrm{Re}_j = 6500$), the RANS modeling overestimates the thermal load at the jet stagnation point significantly.

Correlative approaches to predict the thermal loads due to a single row of impinging jets are difficult to be sorted out from the open literature (see Zuckerman and Lior [27]). In this field, particularly relevant is the contribution of Goldstein and Seol [28] who expressed the Nusselt number Nu on the jet centerline and its decay in the lateral direction as a function of the Re_j and of the geometrical parameters that define the impinging row. Unfortunately, the range of applicability of this correlation ($10{,}000 \leq \mathrm{Re}_j \leq 40{,}000$) falls out the low pressure ACC operating conditions.

As experimental heat transfer investigations are concerned, commonly employed techniques include transient liquid crystal thermography [25] and steady-state thin heating foils, either coupled with thermocouples [29], thermochromic liquid crystals [3] or infrared (IR) cameras [14–17]. Even so, the constraints

imposed by such techniques often lead to a partial lack of similarity with the actual system, which may affect the reliability of the results. In the real hardware, many features have the potential to alter the cooling performance, including target surface properties (e.g., roughness), ACC pipe real geometry (directly affected by manufacturing), wall thermal boundary condition (i.e., hotter-than-air target), and others. None of the aforementioned techniques can be applied if these properties shall be maintained altogether in the experiment. A suitable way to achieve maximum similarity with the actual system is to employ a fully metallic test article, performing both target heating and temperature measurement on the side of the target opposite to the jets, as the employed target distance-to-diameter ratios limit the optical access on jet side. In this case, an inverse heat conduction problem shall be solved in order to retrieve surface heat flux and wall temperature on the target (i.e., opposite) side of the wall. However, a general feature of inverse heat conduction problems is that they are usually ill-posed, i.e., a unique solution might not be present and results may be strongly affected by slight variations of the input data [30]. To address this issue, many methods have been proposed in the open literature, including function specification methods [31], local filtering of input data [32] and regularization methods [30,33]. The selection of the most suitable solution approach is strongly dependent upon the investigated geometry and boundary conditions, and hence, a case by case evaluation must be carried out.

Objectives. As seen from the literature survey previously presented, there is a lack of studies focused on low pressure LPTACC arrangements. When dealing with these cooling architectures, literature correlations for the impingement heat transfer coefficient estimation are out of their confidence range, and also RANS CFD approaches appear not suitable for their design. In this work, methodologies for the development of accurate and reliable tools to determine the heat transfer characteristics of low pressure ACC systems are presented. This paper introduces a finite difference procedure to solve the inverse conduction problem on the target plate. The methodology is applied to an experimental setup for the measurement of the thermal loads on a target plate due to a representative low pressure ACC impinging system. Three different Re_j values were tested in the range of $3800 \leq \mathrm{Re}_j \leq 8200$. Then comparisons with correlative approaches are carried out to prove the methodology consistency at high Re_j (i.e., in the range of applicability of the selected correlations) and to analyze how the results depart from the correlation predictions at low Re_j (i.e., out of the range of confidence of the correlative approach). The experimental data are then used for a preliminary validation of the most suitable CFD approach based on scale-resolving turbulence models.

Modeled Design and Test Matrix

The arrangement investigated in this work consists in a straight pipe facing a flat target plate. The geometrical characteristics of the considered configuration are reported in Table 1 and in Fig. 2.

The manifold tested in this work implements three holes only and is closed at its end. This choice was done to avoid jet deflection effects due to manifold internal crossflow [34]. The main goal of the present contribution, in fact, is to consolidate the experimental methodology against literature correlations. The reduction of the internal crossflow and the related spurious effects permits a cleaner and more dependable comparison between

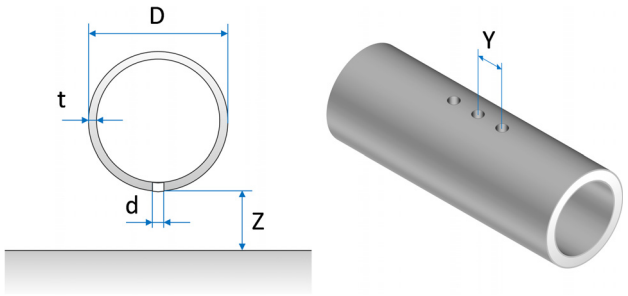

Fig. 2 Geometrical parameters

current results and literature material, which thus strengthens the verification reliability of the proposed approach.

Test conditions were defined by the value of the overall jet Reynolds number, expressed as

$$\mathrm{Re}_j = \frac{\mathrm{md}}{A_{\mathrm{tot}}\mu} \tag{1}$$

where m is the total mass flow rate, d is the hole diameter, and A_{tot} it the overall passage area for the three holes, while μ is the flow dynamic viscosity, evaluated at the jet total temperature. The nominal investigated values of Re_j are reported in Table 2, together with the jet total temperature employed for all tests. The investigated Re_j range allows to validate the employed experimental setup against literature data (since the maximum Re_j value is close to the lower limit of Goldstein and Seol [28] correlation validity range), as well as to investigate the behavior of the system when low mass flow rates are concerned (for the lower Re_j values).

Experimental Methodology

In this section, a suitable experimental methodology for a reliable investigation of ACC systems will be presented. The method is based upon a steady-state investigation of a fully metallic test sample, followed by the solution of an inverse heat conduction problem on the jet target surface to retrieve the system cooling performance. In particular, the use of a metallic sample allows to obtain material and manufacturing similarity with the actual system, especially if a 1:1 scale is adopted. On the other hand, the selection of a steady-state technique instead of a transient one is related to the typical features of ACC systems. In fact, the relevant length of ACC manifold would smooth and alter any flow temperature step applied at the inlet to obtain a transient heat transfer on the target, which is particularly true if a metal ACC pipe is employed. This phenomenon would require a local reconstruction of air temperature in space and time, which is a difficult and often unreliable task. Moreover, since with steady-state technique both local temperature and heat flux can be evaluated, a robust definition of boundary conditions for CFD analyses can be obtained. As so, steady-state technique is recommended for the study of ACC systems and hence was employed for the present investigation.

Experimental Apparatus. In order to perform heat transfer measurements, a suitable test rig was installed in the Heat Transfer and Combustion Laboratory of the Department of Industrial Engineering of the University of Florence (DIEF). The rig, a scheme of which is reported in Fig. 3, is designed in order to

Table 1 Details of the investigated geometry

N° holes	Z/d	Y/d	t/d	D/d	d (mm)
3	5	6	0.5	12	1

Table 2 Operating conditions

Jet Reynolds number	Jet total temperature (K)
3800, 5400, 8200	292

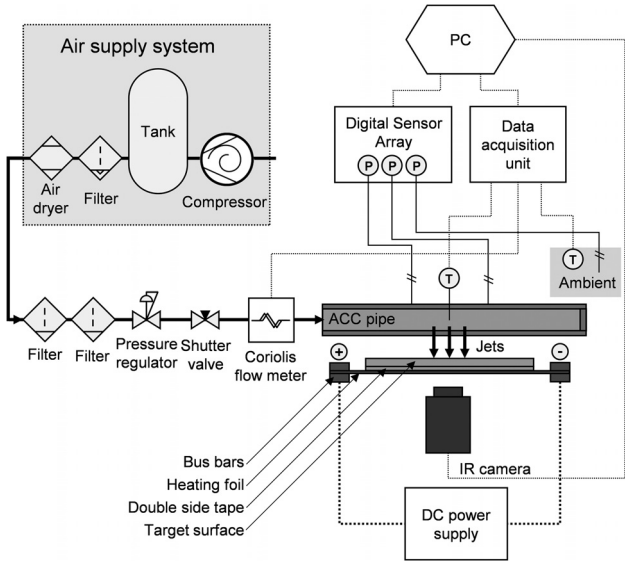

Fig. 3 Scheme of the test rig

replicate the geometry presented in the previous section, as well as to allow the measurement of target wall heat transfer through a steady-state heat transfer technique.

The rig is fed by means of compressed air, which is provided by a suitable supply system. To obtain a pure flow with constant pressure, a filtering section and a pressure regulator are employed. A shutter valve is also installed on the supply line, allowing mass flow regulation.

The main component of the rig is the test section, which actually replicates the cooling geometry. The jet target surface is positioned normal to the impingement holes. The plate itself is a 0.7 mm thick stainless steel plate, 100 mm long, and 60 mm wide. The plate is supported at the end of the longest side, which is aligned with the ACC pipe axis. The orientation of the target surface is horizontal in order to minimize the parasitic effect of the natural convection.

In order to apply the steady-state heat transfer measurement technique, a constant heat flux needs to be applied to the surface, which in this case is obtained thanks to an electrically heated 25.4 μm thick Inconel foil. High temperature resistant double-side tape (0.2 mm thick) is employed to apply the heating foil to the target. In order to preserve the surface properties of the target plate, the heating foil is installed on the side opposite to the jets. Even if this is not within the scope of this work, this solution would allow to study the effect of target properties (e.g., roughness or a specifically designed contouring) on ACC heat transfer. The foil is also 100 mm long and 60 mm wide, but its longest side is perpendicular to the one of the target plate: this results in a $60 \times 60\,\text{mm}^2$ measurement section. The extremities of the heating foil are enclosed within copper bus bars, which in turn are connected to a direct current power supply (N5763A from Agilent, Santa Clara, CA).

The external side of the heat transfer surface (i.e., the one where Inconel is applied) is covered by a thin layer of high emissivity, high temperature black paint, and is observed by means of a SC6700 IR camera from FLIR Systems (Wilsonville, OR). Temperature was sampled on the external surface since a direct measurement on the inner surface is difficult to obtain, given the low Z/d values typical of LPTACC systems and the presence of the pipe. The emissivity of the paint is calibrated by means of a dedicated apparatus, consisting of a painted flat aluminum sample, heated up thanks to a foil heater of the same size and enclosed in insulating foam. Emissivity values were retrieved by targeting the temperature reading of the IR camera with the measurement of a thermocouple embedded in the sample. It was found that the emissivity is independent of both temperature and viewing angle for the ranges employed in the present investigation, and its value is equal to 0.90. It must be added that, since the postprocessing technique presented in the Postprocessing Procedure section is sensible to measurement noise, a high-quality finish needs to be obtained for the measurement surface, avoiding grainy temperature maps and providing smooth gradients. This feature needs to be considered in the selection of the most suitable paint, and should be preferred even to larger emissivity values.

Apart from target temperature, other values need to be recorded to rebuild heat transfer. In particular, flow temperature is sampled inside the tube in a location corresponding to the central jet, while ambient temperature is also recorded on both sides of the target plate in order to evaluate heat losses. These measurements were carried out using type T thermocouples (0.5 K relative accuracy), connected to a data acquisition/switch unit (Agilent 34970 A) and to a temperature controlled cold junction (Pt100, 0.1 K absolute accuracy). Static pressure was also sampled in different locations in order to retrieve the discharge features of the system: in particular, two pressure taps are located inside the ACC pipe (directly upstream and downstream the impingement holes). Pressure is measured by a DSA 3217 scanner from Scanivalve (Liberty Lake, WA) with 15 Pa accuracy. Inlet mass flow rate is directly obtained using a Coriolis mass flowmeter mini CORI-FLOW^{TM} M14 from Bronkhorst (Ruurlo, NL), with 1 g/s range and 0.5% accuracy, which is also connected to the data acquisition unit.

Postprocessing Procedure. Raw experimental data need to be postprocessed in order to retrieve the heat transfer distribution on the inner side of the target plate. In this case, convective heat transfer coefficient h is defined as

$$h = \frac{q_{\text{conv,int}}}{T_w - T_{\text{ad},w}} \tag{2}$$

where $q_{\text{conv,int}}$ is the convective heat flux on the impingement side of the target plate, T_w is the corresponding wall temperature, and $T_{\text{ad},w}$ is the adiabatic wall temperature. The use of $T_{\text{ad},w}$ as reference flow temperature for the definition of h is a common choice in the open literature [28] when recovery factor values significantly different from unity are expected. In the present case, the technique presented by Goodro et al. [14] is employed to retrieve $T_{\text{ad},w}$: tests with three different thermal power levels are performed, and then the zero heat flux temperature (i.e., adiabatic wall temperature) was evaluated by means of linear regression between wall heat flux and wall temperature values. During these tests, it was also verified that the jet total temperature was equal to the ambient one, thus avoiding issues related to the jet entraining the surrounding air. Following this approach, a maximum difference of around 1.2 K between $T_{\text{ad},w}$ and jet total temperature (measured inside the ACC duct) is retrieved in the jet stagnation point.

According to Eq. (2), heat flux and temperature values on the inner surface are required to determine h: however, in this case neither can be directly measured, and only temperature distribution on the outer surface is available. As a consequence, an inverse heat conduction problem on the target surface needs to be solved. To achieve this goal, a finite difference explicit procedure has been developed and applied. The procedure is capable of handling both flat and cylindrical surfaces, built as a wafer of different materials, and for the present case it was implemented in MATLAB. For ease of explanation, only the flat plate case will be treated in the following.

The first step of the procedure consists in discretizing the target surface. In particular, a square mesh is built on the outer surface, housing a node in the geometric center of each element. Mesh sizing can be defined according to the resolution of the input data. The thickness of the target is then also discretized: every layer is divided into one or more sublayers, and a node is placed halfway the thickness of each sublayer in a position corresponding to an

outer node. In other words, assuming that x and y are coordinates defined on the outer surface and z describes the target normal direction, the inner nodes have the same (x,y) coordinates as the outer ones but are located at a different z. Finally, a corresponding grid is also built on the inner surface. An example of the resulting scheme is illustrated in Fig. 4, which corresponds to the configuration adopted in the present case. In particular, in this case grid sizing on the outer surface is 0.2 mm (approximately double the camera mm/pixel resolution) and each material (Inconel, tape, and steel target) is discretized as a single layer. If the surface is cylindrical, the previous discussion can be repeated by replacing x and y with circumferential and axial coordinates.

Once the target is discretized, the measured outer temperature distribution is re-interpolated on the outer nodes. For every element, external heat fluxes are evaluated as

$$q_{\text{conv,ext}} = h_{\text{ext}}(T_{\text{ext}} - T_{\text{amb}}) \tag{3}$$

$$q_{\text{rad,ext}} = \sigma\varepsilon(T_{\text{ext}}^4 - T_{\text{amb}}^4) \tag{4}$$

where h_{ext} is the external convective heat transfer coefficient, σ is Stefan-Boltzmann constant, ε is the external surface emissivity (i.e., the black paint emissivity), T_{amb} is the ambient temperature, and T_{ext} is the external node temperature. For the present investigation, the value of h_{ext} is estimated from literature correlations [35], which is considered satisfactory since external heat flux never exceeds 10% of the internal one. Even so, if required a more reliable estimation of external heat flux could be obtained by insulating the inner surface and performing dedicated heat loss tests.

The sum of external heat fluxes expressed by Eqs. (3) and (4) provides the heat flux toward the exterior of the first element of the first layer, which is also the conductive heat flux from the first internal node to the external node, $q_{\text{cond,ext},2}$. Starting from such value, an element-by-element analysis can be carried out based on local energy balance. In fact, if the generic conductive heat flux toward the outer node $q_{\text{cond,ext},i}$ and the outer node temperature T_{i-1} are known, the temperature of the ith internal node can be expressed as

$$T_i = T_{i-1} + R_{\text{ext},i} \cdot q_{\text{cond,ext},i} \tag{5}$$

where R_{ext} is the external conductive resistance. For the first internal node, R_{ext} is given by only half the thickness of the first sublayer, while for all the other nodes it can be evaluated as the series (i.e., the sum) of the conductive resistances given by half the thicknesses of $(i-1)$th and ith sublayers. For a flat plate, this reduces to

$$R_{\text{ext},i} = \frac{s_{i-1}/2}{k_{i-1}} + \frac{s_i/2}{k_i} \tag{6}$$

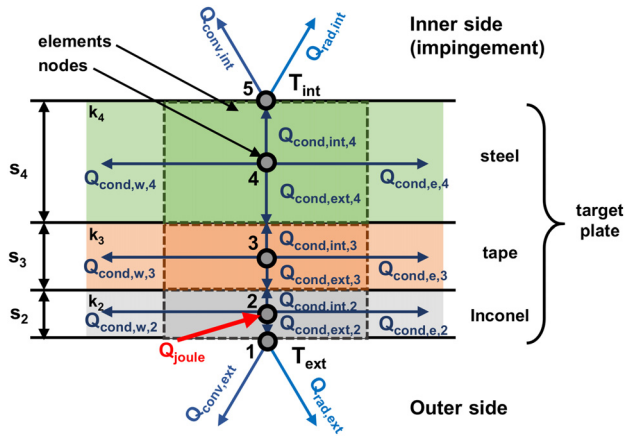

Fig. 4 Target plate discretization

where s is the sublayer thickness and k the conductivity of the corresponding material. Given the relatively low difference between the maximum and minimum temperature of the target (30 K in the worst case), the average thermal conductivity was considered for the present case: even so, a temperature dependant k value should be implemented in the procedure if larger temperature differences would occur across the target material. If Eq. (5) is applied to every node of the ith sublayer, the full temperature distribution of the sublayer is known. This allows to estimate the side heat fluxes occurring in between the elements of the sublayer. As an example, the heat flux toward the northern element is

$$q_{\text{cond},n,i} = \frac{1}{R_{n,i}}(T_i - T_{n,i}) \tag{7}$$

The value of conductive resistance $R_{n,i}$ depends upon the geometry of the plate, but in case of a flat plate with northern direction defined along the x axis it is simply given by $\Delta x/k_i$, where Δx is the node-to-node (uniform) spacing.

One of the main issues related to inverse heat conduction problems is that they are generally ill-posed [30]: as a consequence, the solution might not be unique, and small variations in the input data may result in a strong alteration of the obtained results. On the one hand, this needs the input data quality to be as good as possible (hence the requirements on paint selection). On the other hand, some regularization is needed in order to limit the solution drift toward unrealistic patterns. For this procedure, the most critical aspect was found in the evaluation of lateral heat fluxes, since temperature noise and/or interpolation issues may produce unphysical temperature differences in the right-hand side of Eq. (7), which are then amplified in the evaluation of q_{cond} by the low value of local thermal resistance. For the present case, a suitable way of addressing this issue is to smooth down the side heat fluxes patterns, i.e., the matrices of $q_{\text{cond},n}$, $q_{\text{cond},s}$, etc. values. In this way, single unphysical values are substituted with local averages, hopefully removing the random noise and providing reasonable q_{cond} values. Any smoothing filter with a circular kernel is suitable for this purpose (e.g., moving average or Gaussian): in fact, it can be supposed that thermal properties of each layer are isotropic, hence the smoothing kernel shall perform a direction-independent averaging. The size of the kernel can be easily defined as a tradeoff between the need of preserving the heat transfer pattern shape and the will of limiting the noise in the results: as so, a sensitivity analysis shall be carried out in each case in order to find the most suitable kernel size. For the present case, side heat fluxes are smoothed using a moving average, based on a circular kernel with a radius of 10 elements (i.e., 2 mm, given the mesh sizing).

Since in some layer an internal heat generation might occur, a generated heat $Q_{\text{gen},i}$ also needs to be considered. For the present case, the value for a given element of the Inconel foil is provided by

$$Q_{\text{gen},i} = \text{VI}\frac{G_i}{G_{\text{layer}}} \tag{8}$$

where V and I are voltage and current applied to the heating foil, G_i is the element volume, and G_{layer} is the overall volume of the sublayer. $Q_{\text{gen},i}$ is zero for all of the other layers.

Once all of the heat fluxes are known for a single element, the heat flux $Q_{\text{cond,int}}$ toward the inner surface can be evaluated for a given element by imposing energy balance

$$Q_{\text{cond,ext},i} + Q_{\text{cond},n,i} + Q_{\text{cond},s,i} + Q_{\text{cond},e,i} + Q_{\text{cond},w,i} + Q_{\text{cond,int},i} - Q_{\text{gen},i} = 0 \tag{9}$$

where the single terms are obtained by multiplying the specific heat fluxes per the corresponding element face area. Since $Q_{\text{cond,int},i}$ will be equal to $Q_{\text{cond,ext},i+1}$, it will thus be possible to obtain the temperature of the following sublayer through Eq. (5).

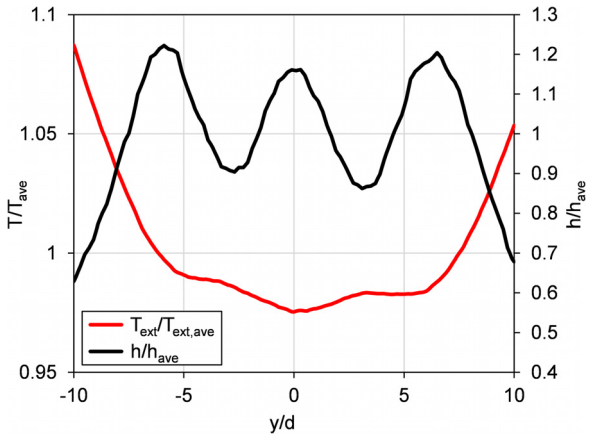

Fig. 5 Dimensionless external temperature and internal convective heat transfer coefficient sampled along the jet stagnation line for $Re_j = 5400$ case

All of the aforementioned operations are repeated for every sublayer until the inner surface is reached. The procedure thus directly provides the temperature distribution on this surface, while convective heat flux $q_{conv,int}$ can be obtained by subtracting the radiative heat flux $q_{rad,int}$ from $q_{cond,int}$. Once this is done, inner h value can be evaluated using Eq. (2). For the present case, the whole procedure takes around 5 s to run.

Despite being based on simple 2D energy balance, the model described in this section offers some valuable characteristics. First of all, the model allows a direct, noniterative solution of inverse heat conduction problems, given that the geometry is sufficiently simple (flat or cylindrical wall). As far as the experience of the authors is concerned, this would be difficult to obtain using a traditional finite element model (FEM) of the geometry, since in this case at least a part of the conditions would need to be specified on every boundary: as a consequence, an iterative boundary update or some kind of parametric characterization of the system [30] would be required to solve the inverse conduction problem. Second, the computational cost of the proposed model is minimal, which is again a significant advantage over full 3D FEM approaches. Finally, the simplicity of the model allows an easy and flexible implementation in a wide variety of cases.

To conclude the description of the proposed methodology, an example of the external wall temperature (i.e., input of the procedure) and internal heat transfer coefficient (i.e., output of the procedure) sampled along the jet stagnation line ($x/d = 0$) are reported in Fig. 5, both scaled with respect to the average value on the same line. In particular, h is evaluated on the jet target (inner) surface, while T is the measured value on the opposite (outer) surface. In the same Figure, $y/d = 0$ is located on the stagnation line of the middle jet. The chart reveals that the evaluation of lateral conduction allows to rebuild intense heat transfer gradients starting from small temperature differences, thus recovering the information smoothed by the large conductivity of the target. This also highlights the need for a particularly sensible temperature measurement device in order to accurately evaluate the magnitude of local temperature gradients: in this case, the sensitivity of the employed IR camera (0.02 K) was found to be satisfactory.

Local h values can be reformulated in a dimensionless form as Nusselt number values

$$\mathrm{Nu} = \frac{hd}{k} \tag{10}$$

where k is air thermal conductivity evaluated at local film temperature.

Uncertainty Evaluation. The uncertainty associated with the obtained Nu values was evaluated using a Monte Carlo approach [36]. This choice is related to the small execution time of the procedure, which allows multiple repetitions to be performed in a reasonable time, as well as to the robustness and ease of application of the method. In particular, the postprocessing procedure was repeated multiple times, and for each repetition, every input was randomly varied within its statistical uncertainty distribution. The point-by-point distributions of the output (i.e., Nu) thus allow to retrieve the local uncertainty, which in this case is evaluated with a 95% confidence level. The number of repetitions is obtained as the one providing the convergence of the method, i.e., additional repetitions would not significantly vary the evaluated uncertainty. For the present case, this is usually achieved with around 5000 repetitions.

Figure 6 presents local uncertainty distributions for the two extreme Re_j values, evaluated on the jet target surface. In both cases, the maximum uncertainty is around 15%; however, for the low Re_j case, it is located far from the stagnation region (identified by the three central peaks) and is mostly related to the uncertainty on the dispersed heat fluxes, due to the large T_w and low internal h values. On the other hand, for the high Re_j case the maximum is in the jets' stagnation region (i.e., where the lowest T_w values occur), and is mainly driven by the uncertainty in temperature measurement.

Uncertainty on Reynolds number was evaluated according to the standard ANSI/ASME PTC 19.1 [37] based on Kline and

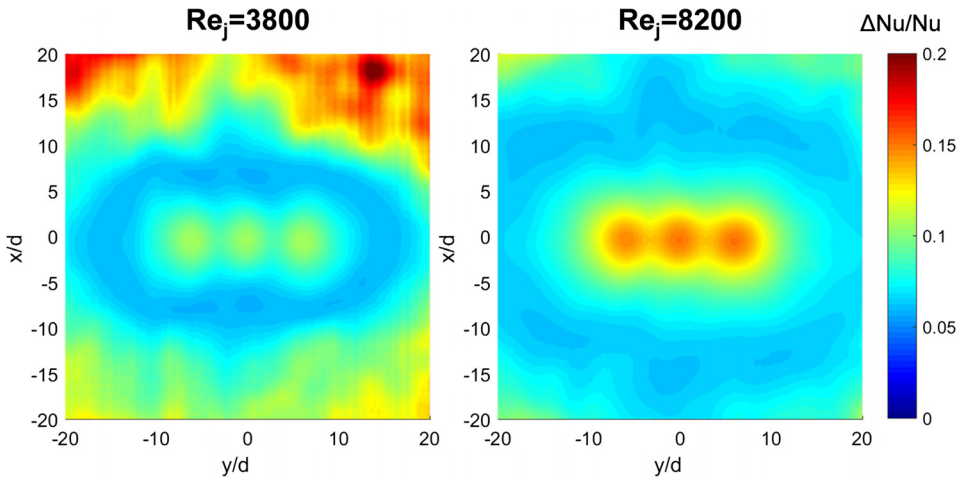

Fig. 6 Uncertainty distributions for the two extreme Re_j values

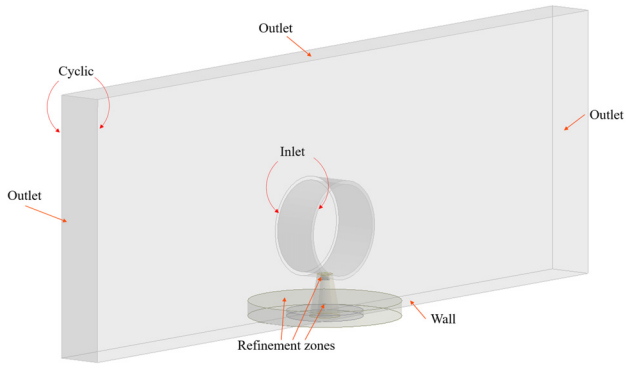

Fig. 7 Computational domain

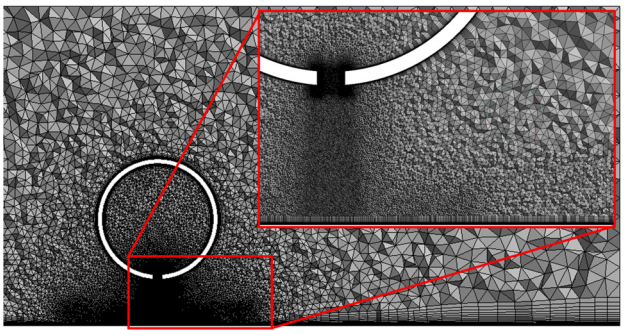

Fig. 8 Computational grid

McClintock method [38]. Maximum uncertainty is recorded for the lowest Re_j value, and is equal to 3.4%.

Computational Fluid Dynamics Methodology

As already mentioned, the presence of only three holes in the array allowed to get rid of the effects of crossflow. The condition was further simplified in the CFD simulations by considering a single hole fed by both sides. This feeding approach does not introduce discharge coefficient or flow field alterations because of the extremely low cross-flow through the manifold [1,2,34].

The computational domain used for the transient simulations is reported in Fig. 7, whereas for RANS cases, the geometric and fluid dynamic symmetry was exploited in order to reduce the computational effort by a factor of 4 and help the convergence of the calculation.

Total pressure and temperature were imposed at the inlets, while a static pressure was imposed at the outlet. Walls were considered as adiabatic and no slip, except for the target plate that was treated with a uniform temperature.

The mesh is shown in Fig. 8. All the grids were generated using 20 prisms, whereas the height of the prism layer was fixed for $x/d < 10$ at 30% of the jet diameter in order to provide an adequate discretization of the developing boundary layer.

Concerning the other numerical settings, air was modeled as an ideal gas with temperature-dependent properties. The turbulence was modeled with the k-ω SST model, with a turbulent Prandtl number for the energy equation of 0.85. The coupled solver was used, while the methods used for discretization were Green-Gauss node based for gradients, second-order for pressure, second-order upwind for momentum and all the other quantities.

When scale-resolving simulations were considered, the stress-blended eddy simulation (SBES) model was chosen, which blends between k-ω SST and dynamic Smagorinsky depending on distance from the wall, mesh sizing and turbulence scales.

In this case, an energy turbulent Prandtl number of 0.5 was used as suggested in Ref. [39]. A synthetic generation of turbulence of 5% was included at the inlet, whereas a nonreflecting condition was added at the outlet. Equations were solved with the SIMPLEC solver, while the methods used for discretization were unaltered, except for the bounded central difference for momentum and bounded second-order for time.

The time-step size was 1×10^{-7} s, which is capable of providing a Courant number close to 1 within the hole. The number of iterations was chosen to provide a reduction in the continuity residuals of two orders of magnitude. The simulated time for the statistical data collection frame was 0.0015 s (about a dozen of flow-through times calculated from the hole to the target plate), whereas additional time was required to flush the initial RANS solution.

The postprocessing of the resulting heat transfer was carried out with a line-averaging process, i.e., for each x/d averaging the solution in the y/d direction. Additionally, for a more practical application also an area-averaging process was considered. For the sake of clarity, an area-averaged value for $x/d = 2$ means that the solution was averaged in the area between $-2 \le x/d \le 2$.

All the computations presented here were obtained exploiting ANSYS FLUENT.

Correlative Approach

The impinging system was also modeled by means of the commercial code flow simulator distributed by Altair. The flow-network illustrated in Fig. 9 represents the actual experimental arrangement and the applied boundary conditions mimic the tests operating conditions.

The impingement holes were modeled as orifices whose discharge coefficient was estimated by means of the routine CDCOMP made available by the solver, which is based on the correlation proposed by McGreehan and Schotsch [40].

Beside the mentioned approach the holes discharge coefficients were estimated also with the correlation by Da Soghe and Andreini [2]

$$C_d = \left(0.745 \cdot \beta^A \cdot \mathrm{E}\right)\left(1 - 1262 \times 3.1^{-8 \cdot \mathrm{MVR}^{0.1124}}\right) \tag{11}$$

where the parameters A and E are given by

$$\mathrm{A} = 0.0124 \cdot \left(\frac{t}{d}\right)^2 - 0.117 \cdot \frac{t}{d} + 0.379 \tag{12}$$

$$E = -0.0204 \cdot \left(\frac{t}{d}\right)^2 + 0.129 \cdot \frac{t}{d} + 0.826 \tag{13}$$

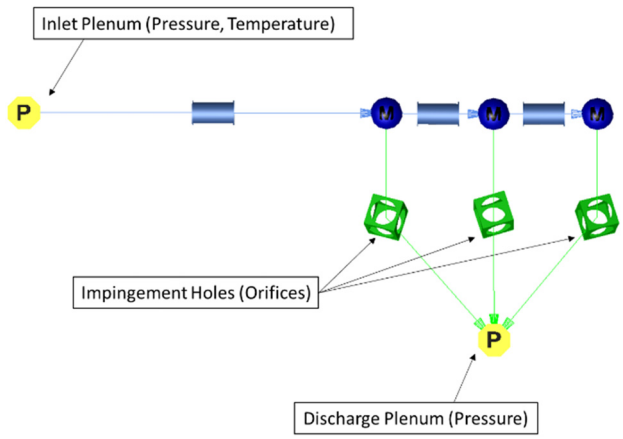

Fig. 9 Flow Simulator fluid-network

and MVR represents the mass velocity ratio $(\rho v)_J/(\rho v)_M$. The aforementioned correlation is valid for $1.01 \leq \beta \leq 1.6$ ($2000 \leq \mathrm{Re}_j \leq 12{,}000$) and $0.25 \leq t/d \leq 3$.

The discharge coefficients calculated by the two correlations and CFD RANS simulations have been reported in Table 3, showing acceptable deviations among the approaches under consideration.

The thermal load on the target surface was estimated by means of the Goldstein and Seol correlation [28]

$$\mathrm{Nu} = \frac{2.9 \cdot \mathrm{Re}_j^{0.7} \cdot \exp\left(-0.09 \cdot \left(\frac{x}{d}\right)^{1.4}\right)}{22.8 + \left(\frac{Y}{d}\right) \cdot \left(\frac{Z}{d}\right)^{0.5}} \tag{14}$$

valid for $10{,}000 \leq \mathrm{Re}_j \leq 40{,}000$, $2 \leq Z/d \leq 8$, $4 \leq Y/d \leq 8$ and $x/d \leq 6$.

It can be noticed that the geometrical parameters of the present geometry completely fit within the correlation applicability range. On the other hand, the investigated Reynolds numbers span from values very close to the minimum of the range ($\mathrm{Re}_j = 8200$) to values far from the minimum ($\mathrm{Re}_j = 3800$). Comparing the results obtained with the largest Re_j value with the outcomes of the correlation will thus allow to reliably validate the employed experimental approach, since it can be expected the correlation to be still valid in the very proximity of the confidence interval. On the other hand, a comparison performed for the smaller Re_j values will allow to assess how the correlative data depart from the measured ones moving away from the correlation range of applicability. The outcomes of these comparisons will be presented in the Results section.

Results

Experimental Results. Figure 10 presents the heat transfer distributions on the target wall obtained with the three Re_j values: 3800, 5400, and 8200. All the presented results were obtained providing the same heat power to the target plate, corresponding to a local average surface heat flux of around 5300 W/m^2. Different heat flux values were also investigated (±50% with respect to the aforementioned value), but no significant effect of this parameter was observed if $T_{\mathrm{ad},w}$ is used to evaluate heat transfer (not shown for the sake of brevity). Every distribution presents three clearly defined peaks, corresponding to the stagnation points of the three jets. The peaks seem almost circular in shape, with only a slight elongation in the spanwise (x) direction. Even if slightly lower heat transfer is recorded for the central peak, in general terms the magnitude of the peaks is similar. As desired, no significant effect of the manifold internal crossflow is visible (see as example Da Soghe and Bianchini [34]). As the distance from the stagnation region increases, heat transfer monotonically decreases. In this region, the Nu distribution seems to protrude more in the x direction for the central jet with respect to the side ones, which is likely to be attributed to flow confinement phenomena. The circular structure on the right-hand side of the distribution is generated by a reference marker point defined on the surface, and so it is ignored in the analysis. As expected, local heat transfer increases with jet Reynolds number, with no significant effect on the shape of the distribution.

Table 3 Comparison of predicted discharge coefficients

Re_j	8200	5400	3800
β	1.217	1.101	1.052
C_d McGreehan and Schotsch [40]	0.715	0.705	0.698
C_d Da Soghe and Andreini [2]	0.702	0.680	0.670
C_d CFD	0.675	0.658	0.651

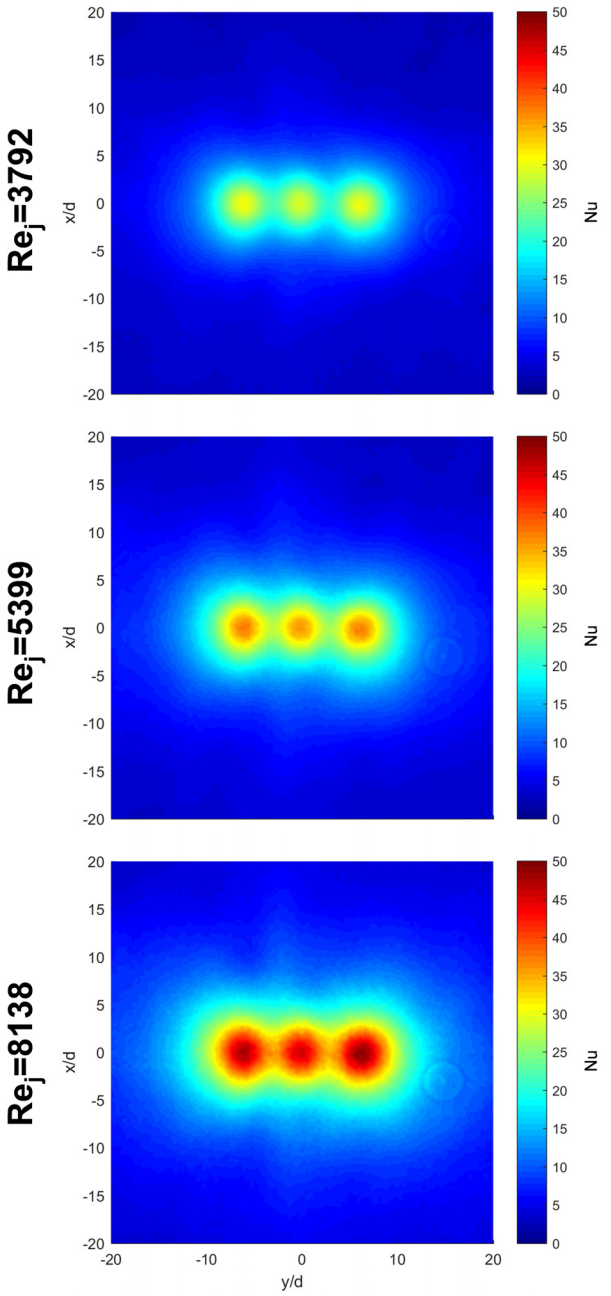

Fig. 10 Heat transfer distributions for the different investigated Re_j values

In Fig. 11 the results obtained with the largest Re_j value are compared with the outcomes of the correlative approach in terms of line averaged Nu values. The experimental values are obtained by isolating the region corresponding to the central jet ($-3 \leq y/d \leq 3$), which can be assumed as representative of a periodic pattern, and averaging Nu values along horizontal lines at different x/d values. The corresponding local experimental uncertainty bands are also reported. As stated previously, since the largest investigated Re_j value ($\mathrm{Re}_j = 8200$) is close to the lower end of the correlation validity range ($\mathrm{Re}_j = 10{,}000$), it can be reasonably supposed that the correlation is still reliable in this condition, and thus its outcomes can be employed for validation purposes. In this case, a pretty good agreement with the predicted values is obtained: in particular, a very good agreement in terms of both values and shape of the distribution is retrieved close to the jet stagnation ($x/d < 4$), with differences largely below the experimental uncertainty. Slightly larger differences are obtained

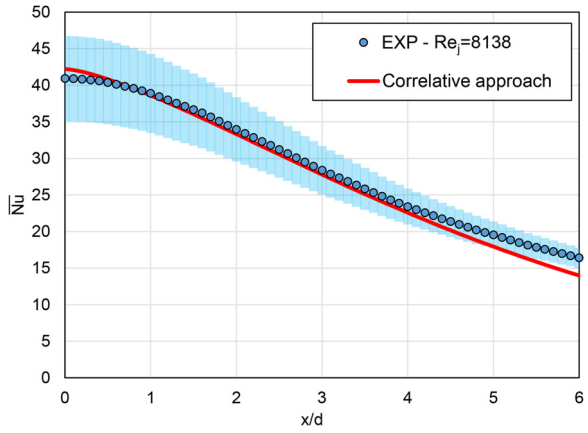

Fig. 11 Comparison between measured and predicted line averaged Nu values for the largest Re$_j$ value

approaching $x/d = 6$, which however is the upper end of the correlation validity range. Given these results, the experimental setup and procedure can be considered as validated.

In order to assess the validity of the correlative approach also for the lower Re$_j$ values, in Fig. 12 the measured values are compared with the predicted ones for all the investigated Re$_j$. In this case, All of the Nu values are scaled with respect to $Re_j^{0.7}$, in order to depurate the results from the effect of this parameter. It must be remembered that, since the correlative approach provides Nu values which are directly proportional to $Re_j^{0.7}$, a single curve is obtained from such approach in all cases.

It can be noticed that moving toward lower Re$_j$ values, i.e., moving away from the validity range of the correlation, the discrepancy in between experimental and predicted values starts increasing, especially close to the jet stagnation ($x/d < 3$). In particular, as Re$_j$ decreases the correlation starts underpredicting the experimental values: in fact, even if such differences are smaller than the experimental uncertainty, a reasonably clear trend can be identified. A possible explanation of this phenomenon may be related to jet flow field: since the correlation was developed for a fully turbulent jet (usually identified with Re$_j > 3000$ [27]), when the jet starts approaching the laminar or transitional region the reliability of the predicted values decreases. This is especially true in the region close to the jet stagnation, where the laminar or turbulent nature of the jet is expected to have an effect on the associated heat transfer. On the other hand, it can be noticed that the three cases behave similarly, and no clear trend can be identified as the distance from the stagnation point increases, since the wall jet is expected to develop a turbulent flow regardless of the nature of impinging jet.

The previous discussion is justified by observing the relationship between measured Nu and Re$_j$ values in different regions. This is illustrated in Fig. 13, where the exponents of Re$_j$ which best represent the local relation between Re$_j$ and Nu with an exponential fit ($Nu = a\ Re_j^b$) are reported. It can be noticed that exponents approaching 0.6 are present close to the jet stagnation ($x/d = 0$), while moving toward the wall jet region (i.e., toward larger x/d values) the exponent increases up to 0.75 and beyond. Since lower values of Reynolds number exponent are associated with laminar flows, Fig. 13 suggests that a behavior approaching the laminar conditions is present close to the jet stagnation for such low Re$_j$ values, while a progressively more turbulent flow is only retrieved as the wall jet develops along the target wall.

Since the laminar behavior of the jet is expected to be emphasized as Re$_j$ decreases, it is likely that moving toward even lower Re$_j$ values the discrepancy between the actual heat transfer values and the ones retrieved through a correlative approach could significantly increase. As a consequence, care should be taken in employing correlations developed for fully turbulent conditions in low Reynolds cases. This finding also justifies the need for dedicated investigations if ACC systems need to be employed with very low Re$_j$ values.

Computational Fluid Dynamics Results. Before comparing the CFD predictions against the already presented experimental and correlative data, it is worth taking a look to the qualitative outcomes of RANS and SBES approaches. An example of the contours of velocity and static temperature for the case at low Re$_j$ are reported in Fig. 14. As it is possible to notice, the RANS prediction returns a very coherent jet, characterized by a very thin shear layer and that keeps most of its velocity to the very proximity of the plate.

After the stagnation, the boundary layer starts developing up to $x/d = 6 - 7$, where a liftoff is observable. The SBES model on the contrary shows a wider jet that immediately after the orifice shows the onset and propagation of large-scale instability waves, which ultimately determine a wider shear layer in time-averaged terms. Additionally, the above-mentioned liftoff phenomenon seems more widespread rather than "frozen" at a given location.

In order to better appreciate in a more quantitative way the impact of such differences on the resulting heat transfer, as well as to benchmark the CFD approach against the experimental data, the Nusselt number was extracted with the same line-averaging postprocessing. The comparison at high Re$_j$ is depicted in Fig. 15. It is evident that the RANS prediction returns a significantly higher Nu at the stagnation point (roughly $+70\%$), which was expected after observing the velocity contours. Similarly, it is possible to notice that some wiggles are present at $x/d \approx 6$, as a consequence of the exacerbated effect of the liftoff returned by RANS. As far as the SBES approach is concerned, interestingly the curve

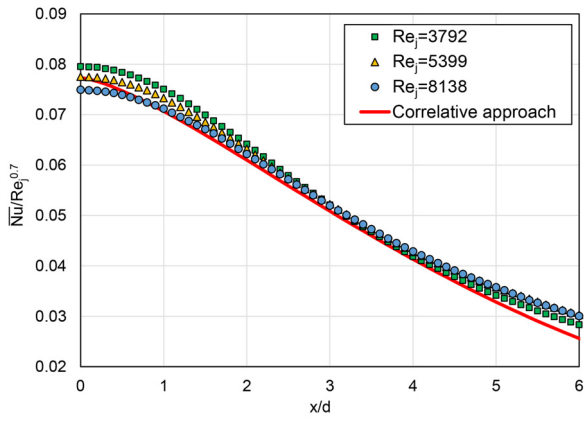

Fig. 12 Comparison between measured and predicted line averaged $Nu/Re_j^{0.7}$ values

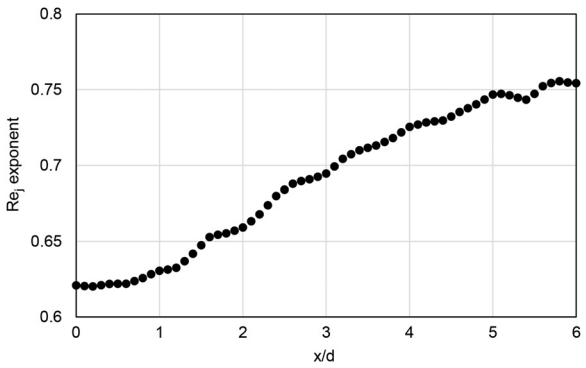

Fig. 13 Exponent of Re$_j$ for the local best fit between line averaged Nu and Re$_j$ ($Nu = a\ Re_j^b$)

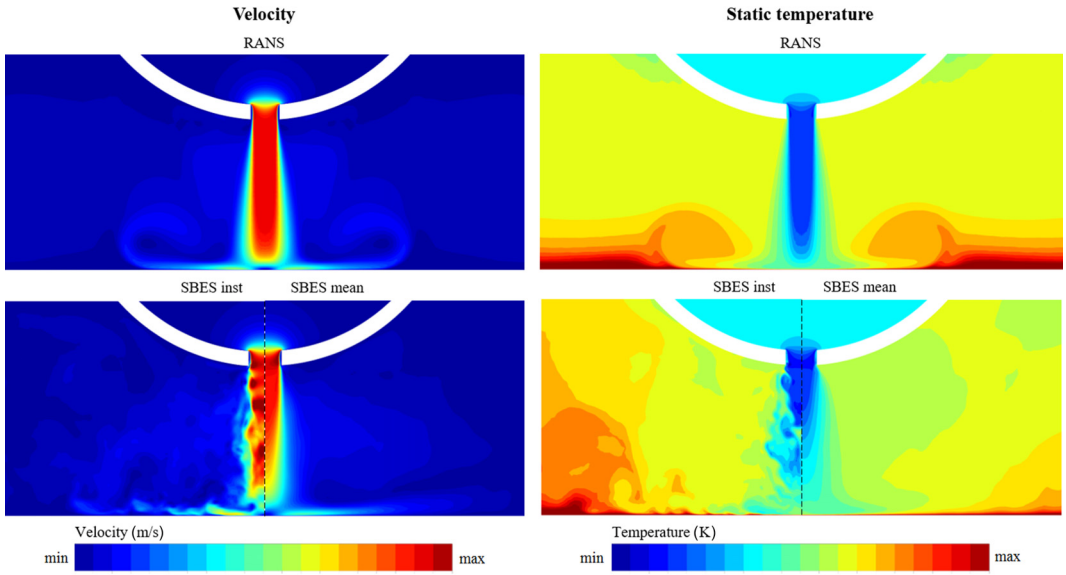

Fig. 14 Contours from RANS compared to instantaneous and mean results from SBES (low Re_j)

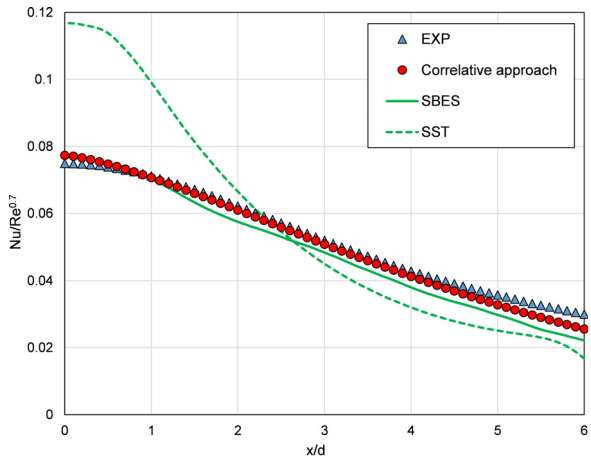

Fig. 15 Line-averaged scaled Nu (high Re_j)

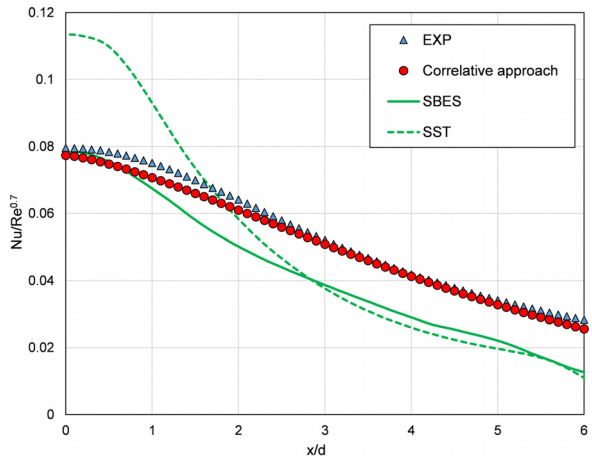

Fig. 16 Line-averaged scaled Nu (low Re_j)

almost overlaps both experimental and correlative predictions for $x/d < 4$, after which it slightly diverges from the experimental data to follow more closely the Goldstein and Seol correlation [28].

When the low Re_j is considered (see Fig. 16), some differences emerge. RANS shows the same overpredicting behavior in the stagnation point, showing also the same intensity. However, the underprediction of the downstream region seems magnified compared to the high Re_j case. SBES seems to match again reference data at the stagnation point, but this time the Nu reduction immediately after that seems steeper, resulting in an increasing underestimation moving downstream. This effect may be evidence of a laminar behavior of the jet which could limit the lateral expansion of the shear layer. It is believed that the effect should not be ascribed to a deficiency of the numerical approach, such as a dissipative effect due to an inadequate mesh or time-step. Since it has proved to be reliable at high Reynolds number in a fully turbulent regime, keeping the same mesh sizing and Courant number, the setup should be able to provide similar or even better capabilities of resolving the turbulence scales. This is confirmed also by Zuckerman and Lior [27], who stated that direct numerical simulation offers little improvements compared to large eddy simulation for laminar flows, since the influence of turbulence is small.

In order to better understand if the phenomena observed are truly representative of a laminar behavior, an additional SBES calculation was performed reducing the feeding total pressure until a reduction of 30% in Re_j was achieved. In Fig. 17, the results obtained using the same scaling principle for the Nusselt number are reported, but considering different values for the exponent of the Reynolds number.

As it is possible to observe, the two SBES curves can be matched using different values for different regions of the plate. Downstream of the stagnation region ($x/d > 1$) the results collapse with an exponent equal to 0.5, a value obtained from the laminar boundary layer theory for a flat exit velocity profile and typically indicated for low-speed flows with a low-turbulence wall jet [27]. However, the stagnation region shows a better matching with a lower exponent equal to 0.3. This value is rather close to what pointed out by Valiorgue et al. [41], who studied impinging synthetic jets with low jet-to-surface spacing and observed a best fitting exponent of 0.32 ± 0.06 in the stagnation region. Additional evidences were provided by Saad et al. [42], who solved the full Navier–Stokes equations and concluded that the Nusselt number was proportional to the $Re_j^{0.36}$ for a parabolic velocity profile and to $Re_j^{0.5}$ for a flat velocity profile in the range $900 < Re_j < 1950$. Such dependency on the inlet velocity profile was highlighted also by Polat et al. [43], indicating a range for the exponent between 0.23 and 0.67.

Therefore, once proved that the SBES calculations are returning a laminar/transitional behavior in the stagnation region, it is worth

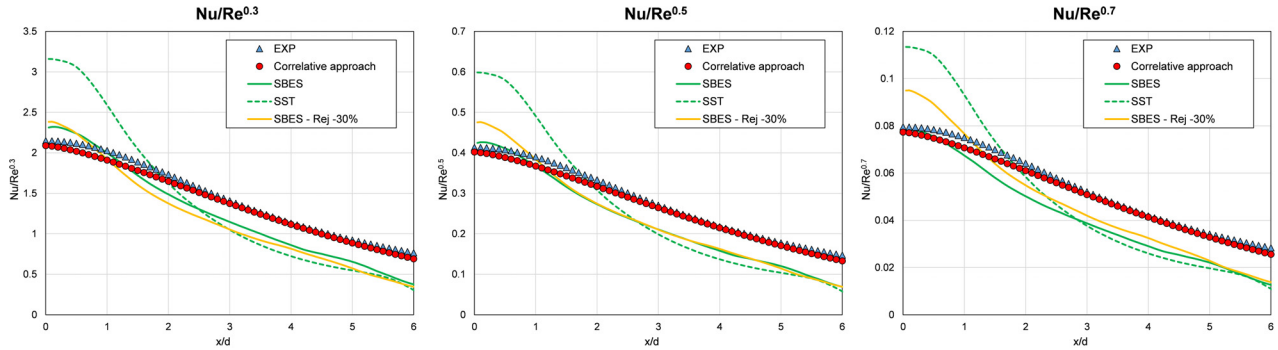

Fig. 17 Effect of jet Reynolds number exponent (low Re_j)

questioning the reasons of such phenomenon. Indeed, the excessive laminarization reproduced by CFD could be an effect of the CFD model itself, that for some reasons does not fully represent the actual experimental conditions. Possible explanation could include the smooth and sharp geometry without potential imperfections due to manufacturing as well as the complete absence of crossflow in the feeding tube. Both assumptions could hinder the onset of the transition to the turbulent regime, keeping the laminar/transitional conditions up to Re_j higher than 3000.

Conclusions

In an attempt to characterize the impact of a reduction in Reynolds number on the performance of ACC systems for future aeroengine, a joint experimental-numerical investigation was carried out. The activity focused on an engine-representative geometry with no-crossflow conditions, so as to validate the experimental approach at high Reynolds number conditions against the correlations available in literature.

Experimental tests were carried out at decreasing Re_j, proving that the heat transfer in the stagnation point gradually approaches values representative of the laminar-transitional conditions, while the region of the developing boundary layer shows a turbulent behavior. This paves the way to future investigations on different test cases at even lower Reynolds number values.

As far as the numerical approach is concerned, as expected using the SST model at high Re_j the heat transfer is overestimated in the stagnation region and underestimated downstream, while the SBES model matches very well the experimental curve. However when considering the low Re_j case, the RANS further intensifies these effects and also SBES starts revealing some limitations.

It was shown that CFD is characterized by a different dependency of Nu on Re_j compared to the experimental tests, highlighting conditions closer to the laminar/transitional regimes. This was ascribed to the model adopted, which considered ideally sharp and smooth surfaces with a total lack of internal crossflow. Both assumptions could lead to a suppression of the onset of transitional effect, limiting the development of turbulent fluctuations and ultimately of the heat transfer. These evidences suggest to further investigate in future activities the role played by manufacturing and feeding conditions at low Reynolds number conditions.

Acknowledgment

This activity was carried out in the framework of the project ACCENTO[3] (Active Clearance Control dEsigN and characTerizatiOn), which has received funding from the Clean Sky 2 Joint Undertaking (JU) under grant agreement N° 831815. The JU receives support from the European Union's Horizon 2020 research and innovation programme and the Clean Sky 2 JU members other than the Union.

The authors thanks Altair to make the software FLOWSIMULATOR available for this study.

Funding Data

- European Commission (Grant No. 831815; Funder ID: 10.13039/501100000780).

Nomenclature

A = area (m^2)
C_d = discharge coefficient, m/m_{is}
d = impingement nozzle diameter (m)
D = manifold diameter (m)
G = volume (m^3)
h = convective heat transfer coefficient ($W\ m^{-2}\ K^{-1}$)
I = current (A)
m = mass flow rate ($kg\ s^{-1}$)
N = number of nozzles in the array
Nu = Nusselt number
P = static pressure (Pa)
q = heat flux ($W\ m^{-2}$)
R = conductive resistance ($m^2\ K\ W^{-1}$)
Re = Reynolds number
t = pipe thickness (m)
T = static temperature (K)
v = jet velocity ($m\ s^{-1}$)
V = voltage (V)
x = spanwise direction (m)
y = streamwise (ACC pipe axis) direction (m)
Y = nozzle-to-nozzle pitch (m)
Z = nozzle-to-plate distance (m)

Greeks Symbols

β = pressure ratio
ε = emissivity
μ = dynamic viscosity ($kg\ m^{-1}\ s^{-1}$)
ρ = density ($kg\ m^{-3}$)
σ = Stefan–Boltzmann constant ($W\ m^{-2}\ K^{-4}$)

Subscripts

ad = adiabatic
amb = ambient
conv = convective
ext = external
is = isentropic
j = jet
m = manifold

[3]https://trimis.ec.europa.eu/project/accento-active-clearance-control-design-and-characterization-advanced-investigations

rad = radiative
tot = overall
u = undercowl
w = wall
0 = total

Acronyms

ACC = active clearance control
CFD = computational fluid dynamics
FEM = finite element model
IR = infrared
LPT = low pressure turbine
MVR = mass velocity ratio $(\rho v)_j/(\rho v)_m$
RANS = Reynolds averaged-Navier–Stokes
SBES = stress blended eddy simulation
SST = shear stress transport

References

[1] Andreini, A., and Da Soghe, R., 2012, "Numerical Characterization of Aerodynamic Losses of Jet Arrays for Gas Turbine Applications," ASME J. Eng. Gas Turbine Power, **134**(5), p. 052504.
[2] Da Soghe, R., and Andreini, A., 2013, "Numerical Characterization of Pressure Drop for Turbine Casing Impingement Cooling System," ASME J. Turbomach., **135**(3), p. 031017.
[3] Andreini, A., Da Soghe, R., Facchini, B., Maiuolo, F., Tarchi, L., and Coutandin, D., 2013, "Experimental and Numerical Analysis of Multiple Impingement Jet Arrays for an Active Clearance Control System," ASME J. Turbomach., **135**(3), p. 031016.
[4] Da Soghe, R., Maiuolo, F., Tarchi, L., Micio, M., and Facchini, B., 2011, "Discharge Coefficient Characterization of Jet Array Impingement Holes for an Active Clearance Control System," ETC 9, Istanbul, Turkey, Mar. 21–25, Paper No. ETC2011-252.
[5] Da Soghe, R., Facchini, B., Micio, M., and Andreini, A., 2012, "Aerothermal Analysis of a Turbine Casing Impingement Cooling System," Int. J. Rotating Mach., **2012**, pp. 1–10.
[6] Da Soghe, R., Bianchini, C., D'Errico, J., and Tarchi, L., 2019, "Effect of Temperature Ratio on Jet Impingement Heat Transfer in Active Clearance Control Systems," ASME J. Turbomach., 141(8), p. 081009.
[7] Da Soghe, R., Bianchini, C., Andreini, A., Facchini, B., and Mazzei, L., 2016, "Heat Transfer Augmentation Due to Coolant Extraction on the Cold Side of Active Clearance Control Manifolds," ASME J. Eng. Gas Turbines Power, **138**(2), p. 021507.
[8] Lefebvre, A. H., 1998, *Gas Turbine Combustion*, Taylor & Francis, Milton Park, Abingdon, UK.
[9] Hay, N., and Lampard, D., 1998, "Discharge Coefficient of Turbine Cooling Holes: A Review," ASME J. Turbomach., **120**(2), pp. 314–319.
[10] Gritsch, M., Schulz, A., and Wittig, S., 1997, "Discharge Coefficient Measurements of Film Cooling Holes With Expanded Exits," ASME Paper No. 97-GT-165.
[11] Gritsch, M., Schulz, A., and Wittig, S., 1998, "Method of Correlating Discharge Coefficient of Film-Cooling Holes," AIAA J., **36**(6), pp. 976–980.
[12] Gritsch, M., Schulz, A., and Wittig, S., 1999, "Effect of Internal Coolant Crossflow Orientation on the Discharge Coefficient of Shaped Film Cooling Holes," ASME Paper No. 99-GT-40.
[13] Rowbury, D. A., Oldfield, M. L. G., and Lock, G. D., 2001, "A Method for Correlating the Influence of External Crossflow on the Discharge Coefficients of Film Cooling Holes," ASME J. Turbomach., **123**(2), pp. 258–265.
[14] Goodro, M., Park, J., Ligrani, P. M., Fox, M., and Moon, H.-K., 2007, "Effects of Mach Number and Reynolds Number on Jet Array Impingement Heat Transfer," Int. J. Heat Mass Transfer, **50**(1–2), pp. 367–380.
[15] Goodro, M., Park, J., Ligrani, P. M., Fox, M., and Moon, H.-K., 2008, "Effect of Hole Spacing on Spatially-Resolved Jet Array Impingement Heat Transfer," Int. J. Heat Mass Transfer, **51**(25–26), pp. 6243–6253.
[16] Goodro, M., Park, J., Ligrani, P. M., Fox, M., and Moon, H.-K., 2009, "Effect of Temperature Ratio on Jet Array Impingement Heat Transfer," ASME J. Heat Transfer, **131**(1), p. 012201.
[17] Goodro, M., Park, J., Ligrani, P. M., Fox, M., and Moon, H.-K., 2010, "Mach Number, Reynolds Number, Jet Spacing Variations: Full Array of Impinging Jets," AIAA J. Thermophys. Heat Transfer, **24**(1), pp. 133–144.
[18] Kercher, D. M., and Tabakoff, W., 1970, "Heat Transfer by a Square Array of Round Air Jets Impinging Perpendicular to Flat Surface Including the Effect of Spent Air," ASME J. Eng. Power, **92**(1), pp. 73–82.
[19] Florschuetz, L., Truman, C., and Metzger, D., 1981, "Streamwise Flow and Heat Transfer Distributions for Jet Array Impingement With Crossflow," ASME J. Heat Transfer **103**(2), pp. 337–342.
[20] Behbahani, A., and Goldstein, R., 1983, "Local Heat Transfer to Staggered Arrays of Impinging Circular Air Jets," ASME J. Eng. Power, **105**(2), pp. 354–360.
[21] Martin, H., 1977, "Heat and Mass Transfer Between Impinging Gas Jets and Solid Surfaces," Adv. Heat Transfer, **13**, pp. 1–60.
[22] Weigand, B., and Spring, S., 2011, "Multiple Jet Impingement - A Review," Heat Trans. Res., **42**(2), pp. 101–142.
[23] Ahmed, F. B., Weigand, B., and Meier, K., 2010, "Heat Transfer and Pressure Drop Characteristics for a Turbine Casing Impingement Cooling System," ASME Paper No. IHTC14-22817.
[24] Ahmed, F. B., Tucholke, R., Weigand, B., and Meier, K., 2011, "Numerical Investigation of Heat Transfer and Pressure Drop Characteristics for Different Hole Geometries of a Turbine Casing Impingement Cooling System," ASME Paper No. GT2011-45251.
[25] Ahmed, F., Poser, B., Schumann, P., Wolfersdorf, Y. J., vonWeigand, B., and Meier, K., 2012, "A Numerical and Experimental Investigation of an Impingement Cooling System for an Active Clearance Control System of a Low Pressure Turbine," International Symposium on Transport Phenomena and Dynamics of Rotating Machinery ISROMAC-14, Feb. 27–Mar. 2, Honolulu, HI.
[26] Marzec, K., and Kucaba-Pietal, A., 2014, "Heat Transfer Characteristics of an Impingement Cooling System With Different Nozzle Geometry," J. Phys. Conf. Ser., **530**, p. 012038.
[27] Zuckerman, N., and Lior, N., 2006, "'Jet Impingement Heat Transfer: Physics, Correlations, and Numerical Modeling'," *Advances in Heat Transfer*, Vol. 39, G. A. Greene, J. P. Hartnett, A. Bar-Cohen, and Y. I. Cho, eds., Elsevier, Amsterdam, NL, pp. 565–631.
[28] Goldstein, R., and Seol, W., 1991, "Heat Transfer to a Row of Impinging Circular Air Jets Including the Effect of Entrainment," Int. J. Heat Mass Transfer, **34**(8), pp. 2133–2147.
[29] Liu, F., Mao, J., Han, X., and Gu, W., 2018, "Heat Transfer of Impinging Jet Arrays on a Ribbed Surface," J. Thermophys. Heat Transfer, **32**(3), pp. 669–679.
[30] Bozzoli, F., Cattani, L., Rainieri, S., Viloche Bazán, F. S., and Borges, L. S., May 2014, "Estimation of the Local Heat-Transfer Coefficient in the Laminar Flow Regime in Coiled Tubes by the Tikhonov Regularisation Method," Int. J. Heat Mass Transfer, **72**, pp. 352–361.
[31] Beck, J. V., and Arnold, K. J., 1977, *Parameter Estimation in Engineering and Science*, John Wiley & Sons, Hoboken, NJ.
[32] Bozzoli, F., Pagliarini, G., and Rainieri, S., 2013, "Experimental Validation of the Filtering Technique Approach Applied to the Restoration of the Heat Source Field," Exp. Therm. Fluid Sci., **44**, pp. 858–867.
[33] Tikhonov, A. N., Goncharsky, A., Stepanov, V. V., and Yagola, A. G., 2013, *Numerical Methods for the Solution of Ill-Posed Problems*, Springer, Berlin, DE.
[34] Da Soghe, R., and Bianchini, C., 2019, "Aero-Thermal Investigation of Convective and Radiative Heat Transfer on Active Clearance Control Manifolds," ASME Paper No. GT2019-90007.
[35] Bergman, T. L., Incropera, F. P., DeWitt, D. P., and Lavine, A. S., 2011, *Fundamentals of Heat and Mass Transfer*, John Wiley & Sons, Hoboken, NJ.
[36] Rubinstein, R. Y., and Kroese, D. P., 2016, *Simulation and the Monte Carlo Method*, John Wiley & Sons, Hoboken, NJ.
[37] ASME, 1985, "Measurement Uncertainty: Instrument and Apparatus," ANSI/ASME PTC 19.1-1985.
[38] Kline, S. J., and McClintock, F. A., 1953, "Describing Uncertainties in Single Sample Experiments," Mech. Eng., **75**, pp. 3–8.
[39] Shum-Kivan, F., Duchaine, F., and Gicquel, L., 2014, "Large-Eddy Simulation and Conjugate Heat Transfer in a Round Impinging Jet," ASME Paper No. GT2014-25152.
[40] McGreehan, W. F., and Schotsch, M. J., 1988, "Flow Characteristics of Long Orifices With Rotation and Corner Radiusing," ASME J. Turbomach., **110**(2), pp. 213–217.
[41] Valiorgue, P., Persoons, T., McGuinn, A., and Murray, D. B., 2009, "Heat Transfer Mechanisms in an Impinging Synthetic Jet for a Small Jet-to-Surface Spacing," Exp. Therm. Fluid Sci., **33**(4), pp. 597–603.
[42] Saad, N. R., Douglas, W. J. M., and Mujumdar, A. S., 1977, "Prediction of Heat Transfer Under an Axisymmetric Laminar Impinging Jet," Ind. Eng. Chem. Fundam., **16**(1), pp. 148–154.
[43] Polat, S., Huang, B., Mujumdar, A. S., and Douglas, W. J. M., "Numerical Flow and Heat Transfer Under Impinging Jets: A Review," Ann. Rev. Heat Trans., **2**(2), pp. 157–197.